nature research

https://doi.org/10.1038/s41550-020-01290-z

Supplementary information

Availability of subsurface water-ice resources in the northern mid-latitudes of Mars

In the format provided by the authors and unedited

Availability of Subsurface Water-Ice Resources in the Northern Mid-Latitudes of Mars

G. A. Morgan[1*], N. E. Putzig[1], M. R. Perry[1], H. G. Sizemore[1], A. M. Bramson[2], E. I. Petersen[2], Z. M. Bain[1], D. M. H. Baker[3], M. Mastrogiuseppe[4,5], R. H. Hoover[6], I. B. Smith[1], A. Pathare[1], C. M. Dundas[7], B. A. Campbell[8]

[1]Planetary Science Institute, AZ, USA.
[2]Lunar and Planetary Lab, University of Arizona, AZ, USA.
[3]NASA Goddard Space Flight Center, MD, USA
[4]California Institute of Technology, CA, USA
[5]University of La Sapienza, Rome, Italy
[6]Southwest Research Institute, CO, USA
[7]U.S. Geological Survey Astrogeology Science Center, Flagstaff, AZ, USA
[8]Smithsonian Institution, DC, USA
* gmorgan@psi.edu

This Supplementary Information PDF file includes:

Supplementary Discussion

Ice-detection technique Methodology

Thermal analysis (*T*): Historically, thermal inertia (TI) has been derived from surface temperature observations using numerical models that assume materials are flat lying and uniform, both laterally (i.e., within the footprint of each observation) and vertically (i.e., within a few seasonal thermal skin depths of the surface) [e.g., 46]. TI values derived this way are most accurately referred to as apparent thermal inertia (ATI). For natural surfaces that exhibit layering, lateral mixing of materials, or significant topography, ATI will vary with time of day and season. These variations can be modeled and compared to ATI values measured over a range of seasons and at different times of day to constrain the style of material heterogeneity at a given location [19; Supplementary Fig. 1]. [23] used this technique to demonstrate that measured ATI values as low as 75 tiu (thermal inertia units: J $m^{-2}K^{-1}s^{-1/2}$) on the polar erg are primarily the result of shallow subsurface ice and not the result of actual low TI surface materials. ATI may also vary substantially with surface slopes, but those in the polar erg contribute only minimally to observed variations in ATI.

Our thermal analysis applies the techniques developed by [19, 23] to search for subsurface ice at lower latitudes. We used ATI derived from both MGS TES and Mars Odyssey THEMIS data. Our forward

models of seasonal ATI variation included various spatial combinations of four thermally distinct type materials representing dust, sand, duricrust, and 'rock'-where 'rock' is thermally indistinguishable from ice and ice-cemented soil. Based on ATI values derived from TES daytime and nighttime data (3-km footprint), we produced a global map of best-fit modeled vertical layering in the upper meter of the Martian surface (Supplementary Fig. 1). We chose 44 targeted locations to perform similar analyses with THEMIS nighttime data, which has finer spatial resolution than TES but coarser spectral and temporal coverage.

We assigned ice consistency values for the TES and THEMIS data separately, using the following criteria. For pixels where model results indicate low TI materials overlying high TI materials (i.e., the dust over rock/ice, dust over duricrust, and sand over rock/ice scenarios represented by blue, green, and cyan pixels in the global layering map), we assigned C_T values of +1. For pixels where model results indicate high TI materials overlying low TI materials (i.e., duricrust over dust, duricrust over sand, and rock over sand; yellow, orange, and red pixels in the global layering map), we assigned C_T values of -1. For pixels where our matching algorithm failed to find a layering scenario consistent with the data, we assigned C_T values of 0. We also assigned C_T values of 0 to locations where the matching algorithm indicated a top layer thickness d less than 1 diurnal skin depth. We made this assignment primarily based on the fact that stable subsurface ice is generally not expected to occur at depths less than 1 diurnal skin depth, even at latitudes between 60° and 80° [e.g., 47]. Identification of very thin material layers also suggests that our two-layer thermal models may not adequately represent more complex subsurface structures at some locations, such as where a thin layer of duricrust might overlie dry sand and deeper ice. Thus, we assigned $C_T = 0$ to all pixels with $d < 1$ diurnal skin depth. We did not assign any fractional consistency values to the TES or THEMIS datasets individually.

Our TES analysis returned a global map of material layering, which we converted directly to a TES consistency map. Our THEMIS analysis focused on 44 regions of interest (ROIs). We created a THEMIS consistency map by assigning 0 consistency to all pixels outside the ROIs. Spatial and temporal data coverage presented a major challenge to applying our techniques to THEMIS data at approximately half of the ROIs. At the locations where our heterogeneity matching algorithm returned results, the top material layer was thinner than the imposed 1 diurnal skin depth minimum—ultimately resulting in an ice consistency value of 0 everywhere in the THEMIS map. We averaged the TES and THEMIS results to produce the final map of C_T used in the SWIM equation. Inclusion of the THEMIS null result effectively limited thermal consistency values to a range 0 – 0.5. We deemed this to be an appropriate scaling of our relative confidence in the thermal results as compared to other data sets, largely driven by the ambiguity between ice and rock for high values of thermal inertia.

We applied the above techniques to produce the thermal data products described in this manuscript, which were publicly released in the spring of 2019. Our methodology continues to be refined and expanded [e.g., 48].

Geomorphic mapping (G): Our geomorphology analysis incorporated previous and new mapping of periglacial and glacial features. Previous work included the location and extent of pedestal craters [49] and mapping of lobate debris aprons, lineated valley fill, and concentric crater fill (LDA/LVF/CCF) [50]. The new mapping component of our analysis focused on tracking the location of 10 distinct landforms and terrain types, inferred to indicate the presence of ice: mantle [15, 51-52], sublimation-type pits, textured terrain, scalloped terrain [e.g., 53], glacial features (i.e., LDA/LVF/CCF and glacier-like forms [GLF]) [e.g. 12, 50, 54], 100-m scale polygons, pedestal craters [49], expanded craters [55], ring-mold craters [e.g., 56-57], and terraced craters [20]. We did not consider 1-20 m scaled polygons [e.g. 58] because these features require HiRISE data to be reliably identified and we used 5 m/pixel CTX data for our mapping. We based our identification of landforms and descriptions on previous work, including recent grid-mapping efforts by [25] and references therein. It should be noted that several of the landforms we identified could be produced by non-ice-related processes, but in aggregate they serve as indicators of ice. We also conducted a more detailed mapping of the presence of scalloped terrain.

To undertake our geomorphic surveys, we applied a modified grid-mapping approach [25]. Here we used polygon shapefiles of the U.S. geological survey geologic map of the northern plains of Mars [59] to define the boundaries of geologic units contained within the study region. We then subdivided the geologic units along 10° lines of latitude and longitude and determined the centroid of each of the subdivided units. Using those centroids, we selected a sample of 4°x4° Mars Reconnaissance Orbiter (MRO) Context Camera (CTX) 5 m/pixel image mosaics (beta01 versions available online from the Caltech Murray Lab at http://murray-lab.caltech.edu/CTX/index.html; see 24) to conduct our survey, the results of which we extrapolated over the entire geologic unit. Although the mosaic is uncontrolled, horizontal errors are expected to be much less than the grid scale.

The 10 landforms discussed above were searched for in the CTX mosaics. We systematically scanned each mosaic at 1:150,000 scale within the boundaries of the map polygons, zooming into the mosaic as needed to investigate individual landforms more closely. Using binary values (1=present, 0=absent), we tallied the occurrence of observed landforms (from the list of 10 above) regardless of their abundance within the image scene. The final geomorphology ice consistency values C_G were calculated using the weighting described in Table S1. For maximum efficiency, we extrapolated this value to the entire polygon.

For landforms that were separately mapped at higher resolution (*i.e.*, LDA/LVF/CCF [50], pedestal craters [49], and scalloped terrain [this work]), we applied weights to the values of C_G based on their expected ice content, with higher weights being applied to features that are currently expected to host significant quantities of ice. The agreement between radar data [e.g. 13] and geomorphic analysis [e.g. 12] strongly supports LDA/LVF/CCF containing present-day glacial ice, and thus these landforms are weighted the highest (pixels containing individually mapped LDA/LVF/CCF are assigned a value of +1). Due to their formation models and the preservation of steep slopes (which in the absence of a binding agent such as ice would be expected to collapse), pedestal craters and scalloped terrain are also considered to contain a higher percentage of ice [49; 60]. Pixels containing these two types of features are assigned a value of +0.75. Expanded craters also similarly indicate high contents [55, 60] but were not separately mapped at high grid resolution across the study region to allow application of the same weighting scheme.

Radar surface analysis (*RS*): To isolate surface radar reflectivity requires that the surface power measured by the radar antenna be normalized for the multiple additional factors that also influence the SHARAD returned signals. To achieve that, we broadly followed a methodology first attempted with MARSIS sounder data [27] while accounting for the higher frequency of SHARAD: (1) to limit the ionosphere effects, we excluded all daytime tracks; (2) we normalized the surface power for the effects of surface roughness using the SHARAD roughness parameter developed by [29]; (3) to account for topographic effects at longer baselines, we corrected for the loss of power due to regional slope using the median MOLA slope value over a Fresnel zone (3 km); and (4) to account for additional MRO influences (spacecraft roll, solar-panel configuration [see 26]), we took the median value of corrected SHARAD returns sampled over bins of 1/12° in longitude and latitude. The final radar-surface ice consistency values C_{RS} were derived from the corrected surface power global distribution as described in Supplementary Table 1.

Radar subsurface analysis (*RD*): SHARAD data are typically represented as radargrams, which are images of returned radar power (represented by pixel brightness) with time delay along the vertical axis and along-track distance along the horizontal axis (Supplementary Fig. 2). The radar wave is reflected from interfaces between materials with contrasting dielectric properties, allowing one to track subsurface interfaces using the measured delay time of returned signals.

When mapping subsurface radar interfaces, it is important to avoid radar "clutter"– signals due to off-nadir surface reflections that occur at similar delay times to subsurface interfaces (Supplementary Fig. 2). We compared each radargram to a MOLA-based topographic clutter simulation [61], and we only mapped as subsurface reflectors those detections that do not have a clutter counterpart.

The relative dielectric constant ($\boldsymbol{\varepsilon}'$), also referred to as the real component of dielectric permittivity, is a material property that controls the propagation velocity of radar waves and can be diagnostic of material composition. Pure water ice at Martian conditions has a dielectric constant of $\boldsymbol{\varepsilon}' \sim 3.15$ [62-63] whereas basaltic materials have higher values of the dielectric constant, $\boldsymbol{\varepsilon}' \sim 6–12$ [64]. Mixtures of materials with different dielectric constants, including added porosity, yield intermediate effective values, which can be estimated using mixing models [e.g., 65-66].

The relative dielectric constant can be estimated following $\boldsymbol{\varepsilon}' = (c\,\Delta t / 2h)^2$, where c = the speed of light, Δt = the two-way delay time between surface and subsurface radar interfaces, and h = the depth to the subsurface radar interface. When a reflecting interface is associated with an identified geologic unit (i.e., a lobate debris apron or plains mantle), the depth to the interface can be estimated from topographic measurements of the unit's surface and margins. We thus estimated h (using MOLA data) for mapped reflectors wherever possible, and together with the measured Δt, we used it to calculate the relative dielectric constant $\boldsymbol{\varepsilon}'$ to constrain the composition and thus possible ice content of relevant geologic units.

The conversion function of $\boldsymbol{\varepsilon}'$ to C_{RD} is shown in Table S1. We selected values of $\boldsymbol{\varepsilon}' = 3$ to correspond to the maximum value $C_{RD} = 1$ (pure ice composition), $\boldsymbol{\varepsilon}' = 5$ to correspond to the equivocal value $C_{RD} = 0$ (could easily be either a rock–ice mixture, high porosity rock, or dust), and $\boldsymbol{\varepsilon}' = 7$ to correspond to the minimum value $C_{RD} = -1$ (likely bedrock with little to no ice content). The value of C_{RD} is thus calculated based on the linear function $C_{RD}(\boldsymbol{\varepsilon}') = \frac{1}{2}(5 - \boldsymbol{\varepsilon}')$ for values of $\boldsymbol{\varepsilon}'$ between 3 and 7 and is fixed at +1 or -1 outside of this range.

Statement on our decision to not incorporate weighting into the SWIM equation (1)

There is an argument for incorporating a weighting scheme into the SWIM equation (1) which would elevate certain techniques over others and/or accentuate returns associated with certain depth ranges (Supplementary Fig. 3). Ultimately, we decided against weighting for three main reasons:

[1] *Philosophical Approach.* Our main goal was to incorporate a diverse range of proxies for the presence of ice and track agreements between them. Under such a framework, we value ice detections derived from multiple data sources above those from a single methodology.

[2] *Lack of Calibration Data.* Ground truth on Mars for the presence of ice is highly limited to a few spot locations, such as the ice-exposing impact sites (Fig. 2) and the Phoenix landing site. Therefore, we do not have the necessary sample size to calibrate the weighting values for each technique (such as might be obtained by using a variance–covariance matrix derived from comparisons between the ground truth and the individual maps).

[3] *Individual technique methodology*. The individual ice consistency values (derived from each technique) are tuned to return high +/- values for measurements consistent with a high likelihood of either the presence or absence of ice. In locations where uncertainty is greater, a lower ice consistency is recorded. As is outlined above and in Supplementary Table 1, to ascertain this value, some of the individual ice consistency calculations incorporate their own weighting schemes. With this in mind, we were reluctant to incorporate additional weighting within equation (1).

All of the constituent ice technique maps (Supplementary Fig. 4) are available on the SWIM website (SWIM.psi.edu) and we encourage members of the community to experiment with their own derivations of the SWIM equation.

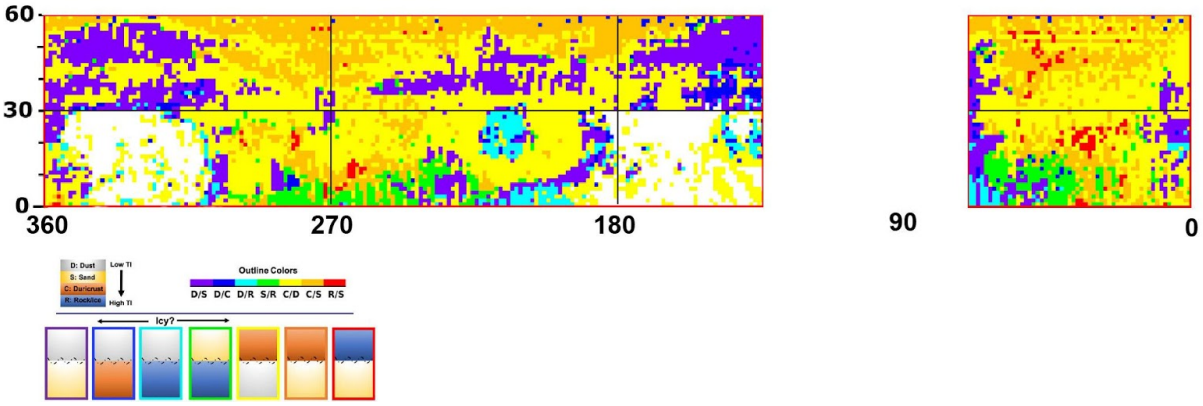

Supplementary Figure 1 TES layered heterogeneity map generated by matching modeled and observed seasonal variations in apparent thermal inertia at 1.25º per pixel. Blue and green pixels indicate a layer of lower thermal inertia material over higher thermal inertia material, which is consistent with the presence of ice and is therefore assigned a value of 1 in the TES component of the ice consistency map. Purple and cyan pixels are also consistent with a low-over-high thermal inertia layering scenario, but the majority of these pixels are assigned 0 in the TES ice consistency map based on the physical requirement that the upper layer must be thicker than 1 diurnal skin depth.

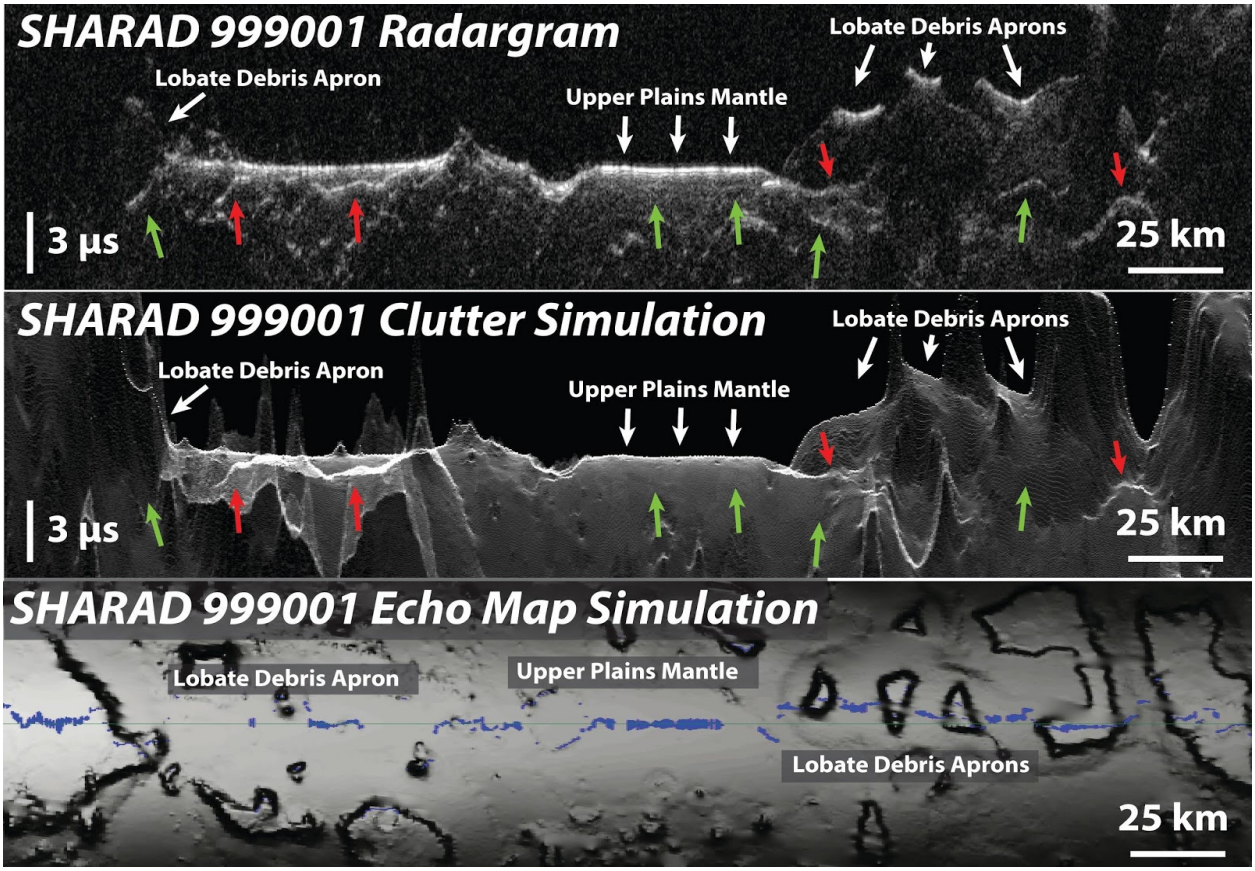

Supplementary Figure 2 Upper panel: Example of a Deuteronilus Mensae SHARAD radargram (collect: 999001). Middle panel: clutter and echo map simulations used to distinguish real subsurface reflections (green arrows) from clutter returns (red arrows). The real subsurface reflectors found below lobate debris aprons are interpreted to be the base of glaciers.

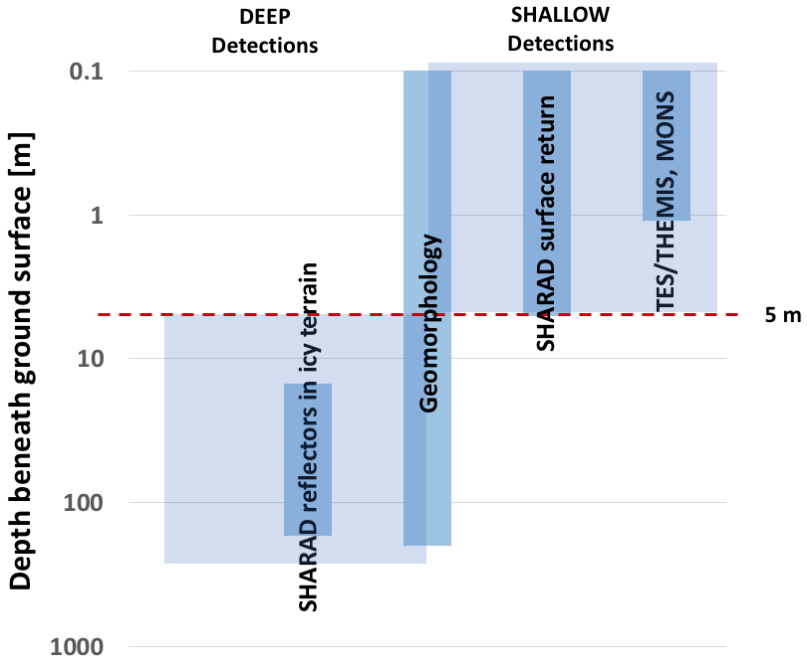

Supplementary Figure 3. Range of sensing depths of each of the ice detection techniques used in the project.

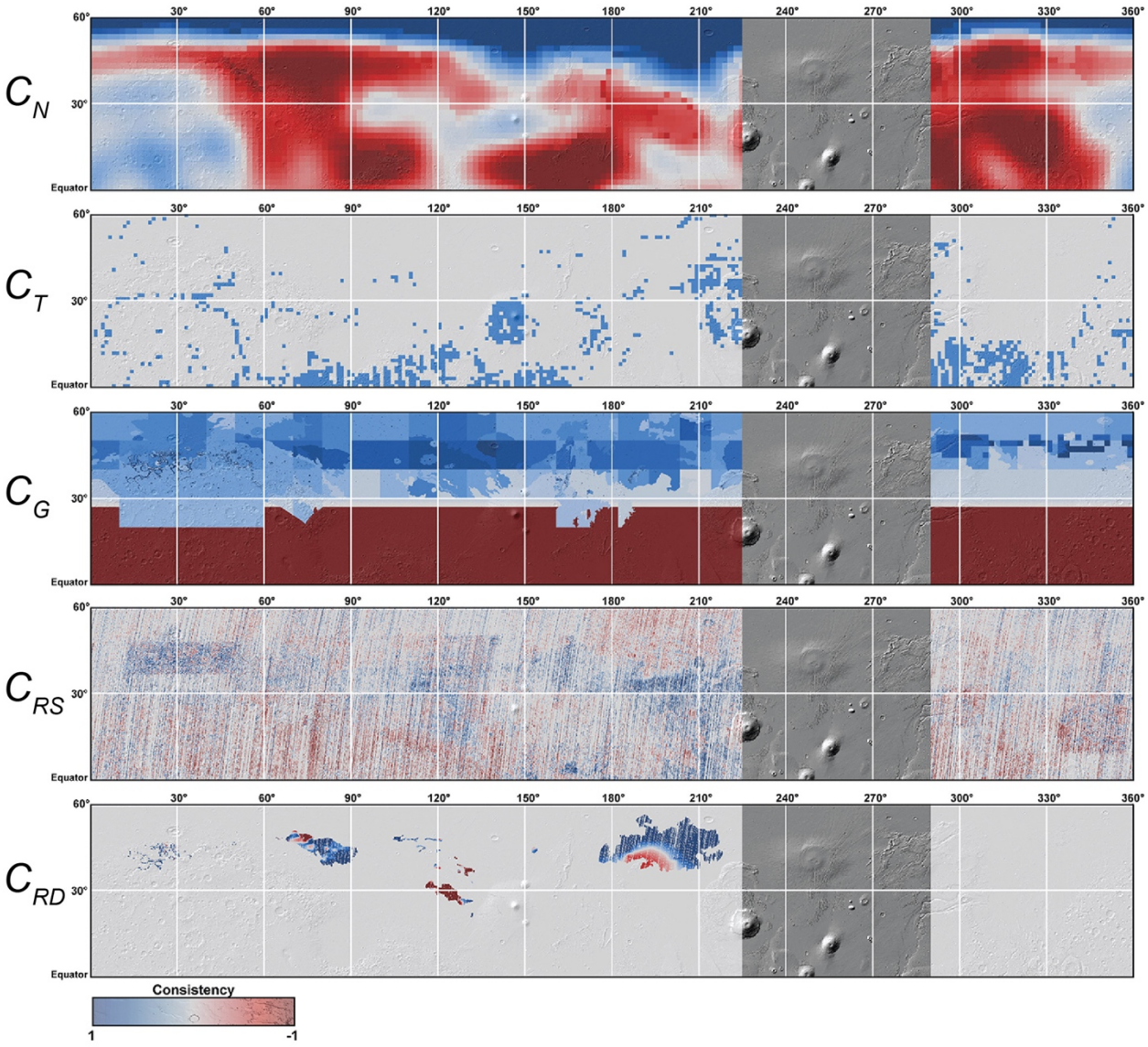

Supplementary Figure 4, The five constituent ice characterization technique maps that provide the input to the Ci map presented in Fig. 1 (via the SWIM equation).

Term	*Datasets*	*Ice Depth (m)*	*How the Term is Calculated*
C_i	All	all	Equation (1)
C_N	Neutron-detected hydrogen in form of ice (MONS)	< 1	C_N = +1 where 25% ≤ W_{dn} C_N is scaled from 0 to +1 where 10% ≤ W_{dn} ≤ 25% C_N is scaled from -1 to 0 where 5% ≤ W_{dn} ≤ 10% C_N = -1 where W_{dn} ≤ 5%
C_T	Thermal behavior consistent with buried ice (TES/THEMIS)	< 1	C_T = +1 where low ATI unit over a high ATI unit C_T = -1 where high ATI unit over a low ATI unit C_T = 0 where no model match OR top layer thickness d < 1 diurnal skin depth
C_G	Ice-related geomorphology (CTX)	all	C_G = max(g_{survey}, $g_{glacial}$, $g_{pedestal}$, $g_{scallop}$) where: g_{survey} = ([mantle] + [sublimation-type pits] + [textured terrain] + [scalloped terrain] + [LDA/LVF/CCF] + [100-m scale polygons] + [expanded craters] + [ring-mold craters] + [pedestal craters] + [terraced craters])/10, with each individual landform yielding +1 where it is present and 0 where it is absent; $g_{glacial}$ = 1.0 where LDA/LVF/CCF mapped [50]; $g_{pedestal}$ = 0.75 where pedestal craters mapped [499]; $g_{scallop}$ = 0.75 where scalloped terrain mapped (new mapping, this study). To reflect the expected decrease in number of periglacial features with increasing proximity to the equator, a Gaussian taper was applied to C_G values from 30° to 27°N, with values declining from 0.1 to 0 in this range. No taper was applied where C_G values were >0.1 below 30°N. The lower latitude bound is based on the equatorward extent of the dissected latitude-dependent mantle [52]. Further, we assigned C_G = -1 to areas <27°N with values max(g_{survey}, $g_{glacial}$, $g_{pedestal}$, $g_{scallop}$) = 0.
C_{RS}	Radar surface returns with ice-like low power (low density) (SHARAD)	< 5	Scaled from the global power distribution such that C_{RS} = +1 where surface power < -1**σ** and C_{RS} = -1 where surface power >1**σ**
C_{RD}	Radar dielectric-constant estimations indicative of ice (SHARAD)	> 15	C_{RD} = +1 where **ε**' ≤ 3 C_{RD} = ½ (5 - **ε**') where 3 ≤ **ε**' ≤ 7 (C_{RD} = 0 where **ε**' = 5) C_{RD} = -1 where **ε**' ≥ 7

Supplementary Table 1. *SWIM equation terms, corresponding instrument datasets, depth sensitivity and the means by which each individual ice consistency term is calculated.*

Latitude	*Longitude*	*Impact Site No.*	*C_i Value*
55.58	150.6	3	0.48
53.27	46.26	10	0.15
52.01	214.7	17	0.28
50.78	208.76	15	0.36
50.37	219.71	16	0.26
46.35	176.89	1	0.21
46.18	188.5	5	0.50
45.06	164.7	4	0.18
44.35	152.93	8	0.13
44.22	164.2	7	0.18
43.9	204.35	14	0.52
43.29	164.21	2	-0.05
39.11	190.25	18	0.23

Supplementary Table 2. *Ice consistency values for each ice exposing impact identified within the study area, ordered by latitude. Impact locations from [17].*

Supplementary References

46. Mellon, M. T., Jakosky, B. M., Kieffer, H. H., Christensen, P. R. (2000). High-resolution thermal inertia mapping from the Mars Global Surveyor Thermal Emission Spectrometer. *Icarus*, 148, 437-455. https://doi.org/10.1006/icar.2000.6503.
47. Schorghofer, N., and Aharonson, O. (2005), Stability and exchange of subsurface ice on Mars, J. Geophys. Res., 110, E05003, doi:10.1029/2004JE002350.
48. Sizemore, H et al., Subsurface Water Ice Mapping (SWIM) on Mars: Thermal and Neutron datasets. 51st Lunar Planet. Sci. Conference Abstract number 2529 (2020).
49. Kadish, S. J., Barlow, N. G., and Head, J. W, Latitude dependence of Martian pedestal craters: Evidence for a sublimation-driven formation mechanism, J. Geophys. Res., 114 (E10). (2009).
50. Levy, J. S., Fassett, C. I., Head, J. W., Schwartz, C., and Watters, J. L. (2014), Sequestered glacial ice contribution to the global Martian water budget: Geometric constraints on the volume of remnant, midlatitude debris-covered glaciers, J. Geophys. Res, 119, 2188– 2196, doi:10.1002/2014JE004685.

51. Mustard, J. F., Cooper, C. D., Rifkin, M. K., Evidence for recent climate change on Mars from the identification of youthful near-surface ground ice. Nature, 1128(1971), 411–414 (2001).
52. Milliken, R. E., Mustard, J. F., and Goldsby, D. L., Viscous flow features on the surface of Mars: Observations from high-resolution Mars Orbiter Camera (MOC) images, J. Geophys. Res., 108, 5057, doi:10.1029/2002JE002005, E6 (2003).
53. Morgenstern, A., Hauber, E., Reiss, D., van Gasselt, S., Grosse, G., and Schirrmeister, L., Deposition and degradation of a volatile-rich layer in Utopia Planitia and implications for climate history on Mars, J. Geophys. Res., 112, E06010, doi:10.1029/2006JE002869 (2007).
54. Milliken, R.E., Mustard, J.F., Goldsby, D.L., Viscous flow features on the surface of Mars: Observations from high-resolution Mars Orbiter Camera (MOC) images. J. Geophys. Res. 108 (E6), 5057, 2003.
55. Viola, D., A. S. McEwen, C. M. Dundas, and S. Byrne (2015), Expanded secondary craters in the Arcadia Planitia region Mars: Evidence for tens of Myr-old shallow subsurface ice, Icarus, 248, 190–204, doi:10.1016/j.icarus.2014.10.032.
56. Kress, A. M., and Head, J. W. (2008), Ring-mold craters in lineated valley fill and lobate debris aprons on Mars: Evidence for subsurface glacial ice, Geophys. Res. Lett., 35, L23206, doi:10.1029/2008GL035501.
57. Baker, D. M. H., & Carter, L. M. (2019). Probing supraglacial debris on Mars 1: Sources, thickness, and stratigraphy. Icarus, 319, 745–769. https://doi.org/10.1016/J.ICARUS.2018.09.001
58. Levy, J., Head, J., and Marchant, D., Thermal contraction crack polygons on Mars: Classification, distribution, and climate implications from HiRISE observations, J. Geophys. Res., 114, E01007, doi:10.1029/2008JE003273 (2009).
59. Tanaka, K.L., Skinner, J.A., Jr., and Hare, T.M., Geologic map of the northern plains of Mars: U.S. Geological Survey Science Investigations Map 2888, scale 1:15,000,000 (2005)
60. Dundas, C. M., Byrne, S., McEwen, A. S. (2015), Modeling the development of Martian sublimation thermokarst landforms. Icarus, 262, 154-169. https://doi.org/10.1016/j.icarus.2015.07.033.
61. Choudhary, P., Holt, J.W., Kempf, S.D.,. Surface clutter and echo location analysis for the interpretation of SHARAD data from Mars. IEEE Geosci. Remote Sens. Lett. 13, 1285–1289. doi:10.1109/LGRS.2016.2581799 (2016)
62. Ulaby, Moore, & Fung (1986) Microwave Remote Sensing, active and passive. Norwood, MA: Artech House.
63. Matsuoka, T., S. Fujita, and S. Mae (1997), Dielectric properties of ice containing ionic impurities at microwave frequencies, J. Phys. Chem. B, 101, 6219–6222, doi:10.1021/jp9631590.
64. Rust, A. C., J. K. Russell, and R. J. Knight (1999), Dielectric constant as a predictor of porosity in dry volcanic rocks, J. Volcanol. Geotherm. Res., 91, 79–96, doi:10.1016/S0377-0273(99)00055-4.
65. Sihvola, A. H. (1999), Electromagnetic Mixing Formulas and Applications, IET.
66. Stillman, D. E., Grimm, R. E., Dec, S. F. (2010), Low-frequency electrical properties of ice-silicate mixtures, J. Phys. Chem. B, 114(18), 6065-6073, doi:10.1021/jp9070778.